THE ASTROPHYSICAL JOURNAL, 239: 622–639, 1980 July 15

STELLAR CONVECTION. II. A MULTIMODE NUMERICAL SOLUTION FOR CONVECTION IN SPHERES[1]

PHILIP S. MARCUS
Center for Radiophysics and Space Research, Cornell University
Received 1979 November 12; accepted 1980 January 17

ABSTRACT

We have computed a stable, equilibrium solution for convection in a self-gravitating sphere of Boussinesq fluid by using a modal analysis in which the θ, ϕ dependence of the fluid is expanded in the set of 168 spherical harmonics, $Y^{l,m}$, with $l \leq 12$. To compute the numerical solution of our hierarchy of nonlinearly coupled equations, we have developed a new relaxation method. For a Rayleigh number that is ~ 30 times critical and a Prandtl number of 10, the flow has two orthogonal planes of reflection symmetry. The temperature, velocity, and convective flux of the fluid as well as the kinetic and thermal energy spectra as functions of wavelength are computed. The spectra are found to be in agreement with both experimental observations and analytic scaling laws. We examine the dynamics of the energy cascade by computing the ratio of the amount of energy dissipation at a particular wavelength to the amount of energy produced at that same wavelength. We find that there is only a slight cascade of kinetic energy to smaller wavelengths but a large cascade of thermal energy. The fraction of the convective flux that is carried by each wavelength and the degree of anisotropy associated with each length scale are also determined. The stable, steady-state convecting fluid has a rotation law such that the angular momentum per unit mass as a function of radius is constant.

Subject headings: convection — hydrodynamics — stars: interiors

I. INTRODUCTION

Thermal convection is perhaps the most important unsolved problem in stellar structure. In 1916 Lord Rayleigh determined the necessary conditions for convective instability using linear theory. Since then, people have been trying to calculate stable, equilibrium solutions to the nonlinear equations of motion. One of the most successful methods is finite amplitude theory (Malkus and Veronis 1958), which can be used to predict the convective flux and temperature gradient for mildly nonlinear, low Reynolds number flows. Recently, Busse (1975) has computed time-independent convective patterns in spheres and spherical shells using this method. Lorenz (1963) considered the self-interaction of a single mode whose radial and horizontal structure was fixed for all time but whose amplitude was allowed to vary. He was able to compute a seemingly "turbulent" time dependence for the convective flux. Toomre, Gough, and Spiegel (1977) have also computed nonlinear solutions by using a single mode whose horizontal structure is fixed but whose vertical structure is determined by the equations of motion. They have been able to calculate convective fluxes that have been applied to the second convection zone of an A star (Toomre *et al.* 1976). Each of these nonlinear methods has produced interesting results, but they are all, obviously, limited to low Reynolds number flows. A severe problem inherent in each method is that it requires *a priori* knowledge of the horizontal structure of the flow. It cannot be determined with these methods which, if any, of the infinite number of possible equilibrium solutions is stable. It is clearly desirable to compare the results of these nonlinear analyses with the solution of a high spatial resolution numerical computation.

In this paper we numerically determine the convective flow of a self-gravitating sphere of Boussinesq fluid for small Reynolds and Peclet numbers. We use the three-dimensional modal analysis that was developed by this author in a previous paper (Marcus 1979, hereafter Paper I). Although the small Reynolds and Peclet numbers are not appropriate for astrophysical flows, their smallness enables us to numerically resolve all of the important physical length scales. This paper is necessary as a foil for the following paper in which we calculate convection for large Reynolds and Peclet numbers, but model the flow at small length scales. The decomposition of the equations of motion into modes is reviewed in § II of this paper, and a relaxation method that allows us to compute solutions to these equations is presented in § III. With this Galerkin method, we are not restricted to small perturbations. By using a wide range of initial conditions and showing that they always evolve to the same steady state, we determine the stable equilibrium flow for a Rayleigh number of 10^4 and a Prandtl number of 10.

[1] Supported in part by National Science Foundation, grants ATM 76-10424 and AST 78-20708, and NASA grant NGR-33-010-186.

In § III we derive different measures that can be used to describe the overall properties of this flow. The two- and three-dimensional spectra of the kinetic and thermal energies and the convective flux as a function of wavelengths are calculated in terms of modes. We also define a measure of the anisotropy of the flow as a function of wavelength. In § IV we present the results of our numerical calculations for our stable convective solution in terms of these measures. Our discussion is in § VI.

II. MODAL EQUATIONS FOR CONVECTION

a) Galerkin Decomposition

The modal equations governing convection in a self-gravitating sphere of Boussinesq fluid were derived in Paper I. In these equations the solenoidal velocity is written as a sum of its poloidal part, $\boldsymbol{v}_p$, and its toroidal part, $\boldsymbol{v}_T$, which are derived from the scalar fields ω and ψ,

$$\boldsymbol{v}_p = \nabla[\partial(r\omega)/\partial r] - (r\nabla^2\omega)\hat{e}_r\,, \tag{2.1}$$

$$\boldsymbol{v}_T = r\nabla \times (\psi\hat{e}_r)\,. \tag{2.2}$$

Each scalar function, $f(r, \theta, \phi, t)$ is written as a sum of its mean or horizontally averaged part, $\langle f(r)\rangle$, and its fluctuating part, $\tilde{f} \equiv f - \langle f\rangle$, where

$$\langle f(r, t)\rangle = \int_{4\pi} d\Omega f(r, \theta, \phi, t)/4\pi\,. \tag{2.3}$$

The fluctuation, $\tilde{f}$, is written as a truncated Galerkin expansion using spherical harmonics:

$$\tilde{f}(r, \theta, \phi, t) = \sum_{l=1}^{l_{\text{cutoff}}} \sum_{m,\gamma} f_{\gamma,l,m}(r, t) Y^{\gamma,l,m}(\theta, \phi)\,, \tag{2.4}$$

where

$$\begin{aligned} Y^{R,l,m} &= 2(2\pi)^{1/2}\,\text{Re}\,(Y^{l,m}) \qquad (m \neq 0) \\ &= 2(\pi)^{1/2} Y^{l,0} \qquad (m = 0)\,, \end{aligned} \tag{2.5}$$

$$\begin{aligned} Y^{I,l,m} &= 2(2\pi)^{1/2}\,\text{Im}\,(Y^{l,m}) \qquad (m \neq 0) \\ &= 0 \qquad (m = 0)\,, \end{aligned} \tag{2.6}$$

and where Re $(Y^{l,m})$ and Im $(Y^{l,m})$ are the real and imaginary parts of the spherical harmonic. The second sum in equation (2.4) is over $0 \leq m \leq l$, and $\gamma = R$ and I. The Galerkin truncation is made by restricting the first sum in equation (2.4) to $l \leq l_{\text{cutoff}}$. We adopt the notation that $\langle\langle f(r)\rangle\rangle$ is the stationary value of $\langle f(r, t)\rangle$; that is, if τ is a period of time that is long compared to the time scales over which $\langle f(r, t)\rangle$ changes, then

$$\langle\langle f(r)\rangle\rangle \equiv \frac{1}{\tau}\int_0^{\tau} \langle f(r, t)\rangle dt\,. \tag{2.7}$$

If the value of $\langle\langle f\rangle\rangle$ depends upon the origin of time used on the right-hand side of equation (2.7), then $\langle f(r, t)\rangle$ is not a stationary function and $\langle\langle f\rangle\rangle$ is undefined.

We shall consider a Boussinesq fluid with a thermal expansion coefficient α, a kinematic viscosity ν, heat capacity c_p, a thermal diffusivity κ, and a mean density ρ. The heat source is $H(r)$, and the steady-state luminosity, $\mathscr{L}(r)$, is

$$\mathscr{L}(r) = 4\pi \int_0^r \langle H\rangle r'^2 dr'\,. \tag{2.8}$$

We nondimensionalize the equations of motion by using the radius of sphere, L, as the unit of length, ρL^3 as the unit of mass, L^2/κ as the unit of time, and $\mathscr{L}(L)/4\pi\rho c_p L\kappa$ as the unit of temperature. In these units the equations that govern the velocity, temperature T, pressure P, and gravitational potential Φ are

$$\begin{aligned} \partial\omega_{\gamma,l,m}/\partial t = &-r[l(l+1)]^{-1}[\text{RsPr}rT_{\gamma,l,m} + \partial(P_{\gamma,l,m} + \Phi_{\gamma,l,m})/\partial r] \\ &+ \text{Pr}\mathscr{D}_l(\omega_{\gamma,l,m}) - l(l+1)^{-1}\{r\hat{e}_r\cdot[(\boldsymbol{v}\cdot\nabla)\boldsymbol{v}]\}_{\gamma,l,m}\,, \end{aligned} \tag{2.9}$$

$$\partial\psi_{\gamma,l,m}/\partial t = \text{Pr}\mathscr{D}_l(\psi_{\gamma,l,m}) - l(l+1)^{-1}\{r\hat{e}_r\cdot\nabla\times[(\boldsymbol{v}\cdot\nabla)\boldsymbol{v}]\}_{\gamma,l,m}\,, \tag{2.10}$$

$$\partial T_{\gamma,l,m}/\partial t = \mathscr{D}_l(T_{\gamma,l,m}) - l(l+1)(\partial\langle T\rangle/\partial r)\omega_{\gamma,l,m}/r - [\boldsymbol{v}\cdot\nabla T]_{\gamma,l,m}\,, \tag{2.11}$$

$$\mathscr{D}_l(P_{\gamma,l,m}) = \text{PrRs}(6T_{\gamma,l,m} + r\partial T_{\gamma,l,m}/\partial r) - r^{-2}\partial\{r[r\hat{e}_r\cdot(\boldsymbol{v}\cdot\nabla)\boldsymbol{v}]_{\gamma,l,m}\}/\partial r - \{\nabla\cdot[(\boldsymbol{v}\cdot\nabla)\boldsymbol{v}]\}_{\gamma,l,m}\,, \tag{2.12}$$

$$\mathscr{D}_l(\Phi_{\gamma,l,m}) = -3\mathrm{PrRs}T_{\gamma,l,m}\,, \tag{2.13}$$

$$\langle\omega\rangle = \langle\psi\rangle = 0\,, \tag{2.14}$$

$$\frac{\partial\langle T\rangle}{\partial t} = r^{-2}\left\{\partial(r^2\partial\langle T\rangle/\partial r)\partial r + \partial\mathscr{L}/\partial r - \partial\left[\sum_{\gamma,l,m} rl(l+1)T_{\gamma,l,m}\omega_{\gamma,l,m}\right]\Big/\partial r\right\}, \tag{2.15}$$

where $\mathscr{D}_l$ is the second-order differential operator defined by its action on f,

$$\mathscr{D}_l(f) \equiv [\partial^2(rf)/\partial r^2 - l(l+1)f/r]/r\,. \tag{2.16}$$

The subscript γ stands for either I or R. The nonlinear terms $\{r\hat{e}_r\cdot\nabla\times[(\boldsymbol{v}\cdot\nabla)\boldsymbol{v}]\}_{\gamma,l,m}$, $[(\boldsymbol{v}\cdot\nabla)T]_{\gamma,l,m}$, $[\hat{e}_r r\cdot(\boldsymbol{v}\cdot\nabla)\boldsymbol{v}]^{\gamma,l,m}$, and $\nabla\cdot[(\boldsymbol{v}\cdot\nabla)\boldsymbol{v}]_{\gamma,l,m}$ are explicitly expressed in terms of $\omega_{\gamma,l,m}$, $\psi_{\gamma,l,m}$, and $T_{\gamma,l,m}$ in Paper I. The Prandtl number, $\mathrm{Pr} \equiv \nu/\kappa$, and the Rayleigh number, $\mathrm{Re} \equiv \alpha GL^3\mathscr{L}(L)/3\kappa^2\nu c_p$ (where G is the gravitational constant) are the two constants that appear in equations (2.9)–(2.15).

b) *Boundary and Initial Conditions*

The boundary conditions are that the surface of the convecting fluid is impermeable and stress-free. This requires that

$$\omega_{\gamma,l,m}(1) = 0\,, \tag{2.17}$$

$$\partial^2\omega_{\gamma,l,m}/\partial r^2|_{r=1} = 0\,, \tag{2.18}$$

$$\partial(\psi_{\gamma,l,m}/r)/\partial r|_{r=1} = 0\,. \tag{2.19}$$

The surface has no thermal resistivity and is therefore isothermal, or

$$T_{\gamma,l,m}(1) = 0\,. \tag{2.20}$$

We are also free to fix $\langle T\rangle$ to be constant for all time at the surface. Since the specific value of $\langle T(1)\rangle$ has no effect on $\boldsymbol{v}$, $\tilde{T}$, $\tilde{P}$, $\tilde{\Phi}$, or $\partial\langle T\rangle/\partial r$, we set it equal to zero:

$$\langle T(1)\rangle = 0\,. \tag{2.21}$$

We have chosen the heat source so that it has a constant value for $r \le 0.3$ and is zero outside $r = 0.3$. In dimensionless units,

$$\tilde{H} = 0\,, \tag{2.22}$$

$$\langle H\rangle = 3/4\pi(0.3)^3 \quad (r \le 0.3)$$
$$= 0 \quad (r > 0.3)\,. \tag{2.23}$$

This heat source produces a steady state luminosity,

$$\mathscr{L}(r) = (r/0.3)^3 \quad (r \le 0.3)$$
$$= 1 \quad (r > 0.3)\,. \tag{2.24}$$

The total heat flux (per unit area) at the surface is $-\partial\langle T\rangle/\partial r$ and is free to vary in time. The thermal and kinetic energy can be stored in the fluid and released through the surface in a series of bursts rather than in a continuous flow. However, $\langle\langle\partial T/\partial r\rangle\rangle = -1$.

No boundary conditions are imposed at the center of the sphere, but regularity requires that leading order terms of $\omega_{\gamma,l,m}$, $\psi_{\gamma,l,m}$, $T_{\gamma,l,m}$, $P_{\gamma,l,m}$, and $\Phi_{\gamma,l,m}$ all go as r^l at the origin. The dipole component of the velocity may be nonzero at $r = 0$.

III. ARTIFICIAL TIME METHOD OF SOLUTION

A straightforward method of obtaining solutions to equations (2.9)–(2.15) is to choose some initial data and integrate the equations forward in time. However, we have developed a relaxation scheme, the method of artificial time, that determines convective solutions in a more efficient manner.

a) *The Initial-Value Problem In Real Time*

Consider a fluid with its mean temperature in conductive equilibrium,

$$\langle T\rangle = r/(0.3)^3 \quad (r \le 0.3)$$
$$= 1/r^2 \quad (r > 0.3)\,, \tag{3.1}$$

TABLE 1

CRITICAL VALUES OF THE RAYLEIGH NUMBER, $Rs_{crit}(l)$, AT WHICH EIGENMODES OF WAVENUMBER l BECOME UNSTABLE

l	1	2	3	4	5	6	7	8	9	10	11	12
$Rs_{crit}(l)$	296	759	1702	3329	5869	9583	14759	21715	30792	42353	56809	74577

and with velocity and temperature fluctuations that are initially small. If the Rayleigh number is sufficiently large, ω and T initially grow almost exponentially. We can understand this growth by computing the linearized eigenmodes to equations (2.9)–(2.15); $\omega_{\gamma,l,m}$ and $T_{\gamma,l,m}$ grow (decay) if Rs is greater (less) than the critical Rayleigh number, $Rs^{crit}(l)$. The growth and decay rates are independent of γ and m. The toroidal component of the velocity always decays initially. $Rs_{crit}(l)$ is given in Table 1.

If $Rs < Rs_{crit}(l)$, then the velocity decays and the mean temperature remains unchanged. (We have not found a numerical example of subcritical, finite-amplitude convection.) The initial growth rate of each eigenmode increases with increasing Rs as do the l-values of the most unstable modes. For example, $l = 6$ is the most unstable eigenmode for $Rs = 10^8$. Although $\tilde{T}$ and ω grow rapidly, $\langle T \rangle$ changes very slowly and its growth rate is determined by the conductive time scale, which is $\sim 10^{-5}$ of the growth rates of $\tilde{T}$ and ω for $Rs = 10^8$. The horizontally averaged temperature does not begin to change appreciably until the convective flux, $\langle \tilde{T} v_r \rangle$, is of the same order as the steady-state flux, $\mathscr{L}/r^2$. The mean temperature gradient then becomes nearly isothermal (isothermal $\equiv$ adiabatic for a Boussinesq fluid). At this point, the velocity is large and chiefly made up of the most unstable eigenmodes (large l) of the conductive temperature gradient. The nearly isothermal temperature gradient is not in equilibrium with a velocity field with these characteristics. For steady-state equilibrium with a nearly isothermal temperature gradient, the velocity must be made up of the neutrally stable eigenmodes of that same temperature gradient (*not* the conductive gradient). The latter eigenmodes are characterized by smaller values of l than the unstable eigenmodes of the conductive gradient. Therefore the velocity begins cycles of decay and growth, with lower and lower values of l dominating the velocity until a statistically steady state is reached. The integration of the velocity forward in time is limited by a Courant condition; a large velocity requires a small time step. Because the time step must be small and because the velocity and temperature must cycle through many states until they reach a statistically steady state, finding solutions by integrating equations (2.9)–(2.15) forward in time is inefficient.

b) The Initial-Value Problem in Artificial Time

Instead of integrating the equations of motion in real time, we can force the fluid to go through a series of states in which the mean temperature gradient is always in instantaneous equilibrium with the velocity field and convective flux. The only modification to the equations of motion (2.9)–(2.15) is to set $\partial \langle T \rangle / \partial t = 0$ or equivalently to replace equation (2.15) with

$$\frac{\partial \langle T \rangle}{\partial r} = -\mathscr{L}(r)/r^2 + \sum_{\gamma,l,m} T_{\gamma,l,m} \omega_{\gamma,l,m} l(l+1)/r \,. \tag{3.2}$$

With this modified set of equations, $\tilde{T}$, $\tilde{\omega}$, and $\partial \langle T \rangle / \partial r$ all initially grow exponentially. Within a few eddy-turnover times the solution converges to a statistically steady state. Any solution to the artificial time equations (2.9)–(2.14) and (3.2) in which $\partial \langle T \rangle / \partial r$ does not change in time is also an exact equilibrium solution to the real time equations, although it is not necessarily a stable solution. Stability is tested by adding a perturbation to the equilibrium solution, integrating it forward in real time, and testing to see whether the perturbations grow or decay. Regardless of the amplitude of the perturbation, we have never found a time-independent solution generated from the artificial time equations that was unstable in real time.

Sometimes the artificial time equations converge not to a steady state but only to a statistically steady state (in which the mean temperature gradient, heat flux, and spectra of the kinetic energy and thermal fluctuations are stationary). In these cases the variations in time of $\partial \langle T \rangle / \partial r$ are small, but they do not have the same time dependence that $\partial \langle T \rangle / \partial r$ has in real time (see Marcus 1980). If the statistically steady artificial time solutions are used as the initial data in integrating the equations in real time, the solution converges to a new statistically steady state in only a few eddy-turnover times.

IV. DESCRIPTION OF THE FLOW

In our modal representation of the fluctuating quantities, we have chosen $l_{cutoff} = 12$, which requires 168 modes (γ, l, m). By using a radial grid of 128 zones, each scalar is represented by 21,504 numbers. It therefore becomes important to decide which quantities should be calculated to describe the flow in a sensible manner.

a) The Temperature Gradient and Mean Thermal Energy

The rate of change of the mean thermal energy of the fluid is determined by integrating equation (2.15) twice over the entire radius of the sphere:

$$\partial\left[\int \langle T\rangle dr^3\right]\Big/\partial t = 4\pi\int_0^1 \langle H\rangle r^2 dr + 4\pi\left.\frac{\partial\langle T\rangle}{\partial r}\right|_{r=1}. \tag{4.1}$$

The first term on the right-hand side of equation (4.1) is the rate at which energy is pumped into the fluid from the heat source; the second term is the rate at which energy is conducted away from the surface of the sphere. If the integration of equation (2.15) is left as an indefinite integral, we obtain the equation for the mean thermal heat flux:

$$-\frac{\partial\langle T\rangle}{\partial r}\partial r + r^{-1}\sum_{\gamma,l,m} T_{\gamma,l,m}\omega_{\gamma,l,m} l(l+1) + \frac{\mathscr{L}(r)}{r^2} = -r^{-2}\partial\left(\int_0^r dr' r'^2\langle T\rangle\right)\Big/\partial t\,. \tag{4.2}$$

The first term on the left-hand side of equation (4.2) is the conductive heat flux, and it is therefore important for us to compute the mean temperature gradient. The second term on the left-hand side of equation (4.2) is the convective flux $F_{\rm con}$. Each mode, (γ, l, m), contributes to the flux with no cross terms between modes. We will find it useful to consider the convective flux carried by all modes with a particular value of l, $F_{\rm con}(l)$:

$$F_{\rm con}(l) = r^{-1} l(l+1)\sum_{\gamma,m}\omega_{\gamma,l,m} T_{\gamma,l,m} \tag{4.3}$$

with

$$F_{\rm con} = \sum_l F_{\rm con}(l)\,. \tag{4.4}$$

The third term on the left-hand side of equation (4.2) is the heat flux of the steady-state fluid. The right-hand side of equation (4.2) is the rate at which the stored thermal energy is being released.

b) Energy Spectra in Two and Three Dimensions

The kinetic energy per unit mass in a shell of radius r is (see Paper I):

$$\mathrm{KE}(r) = \sum_l \mathrm{KE}(l, r) \tag{4.5}$$

with

$$\mathrm{KE}(l, r) = \tfrac{1}{2} l(l+1)\sum_{\gamma,m}\{\omega_{\gamma,l,m}{}^2 l(l+1) + [\partial(r\omega_{\gamma,l,m})/\partial r]^2\}/r^2 + \psi_{\gamma,l,m}{}^2\,, \tag{4.6}$$

where $\mathrm{KE}(l, r)$ is the kinetic energy due to all modes, (γ, l, m), for all γ and m. Similarly we can define a fluctuating thermal energy:[2]

$$\mathrm{TE}(r) \equiv \tfrac{1}{2}\langle\tilde{T}^2\rangle = \sum_l \mathrm{TE}(l, r) \tag{4.7}$$

with

$$\mathrm{TE}(l, r) = \tfrac{1}{2}\sum_{l,m}\tilde{T}_{\gamma,l,m}{}^2\,. \tag{4.8}$$

Traditionally one calculates the fluctuating thermal energy and the kinetic energy spectra as functions of a three-dimensional wave number, whereas $\mathrm{TE}(l, r)$ and $\mathrm{KE}(l, r)$ are functions of radius and the two-dimensional wavenumber l. In a bounded spherical geometry it is more natural to compute these two-dimensional spectra. Three-dimensional spectra are better suited to an unbounded or periodic Cartesian geometry. To compare our results with other published work, we show in the Appendix how to transform our two-dimensional spectra into three-dimensional spectra.

c) Total Energy Budgets

Multiplying the Boussinesq Navier-Stokes equation by the velocity and integrating over the volume, we obtain the kinetic energy budget:

$$\partial\left[\frac{1}{2}\int dr^3 v^2\right]\Big/\partial t = 4\pi\mathrm{PrRs}\int_0^1\langle v_r T\rangle r^3 dr - \mathrm{Pr}\int dr^3\left(\frac{\partial v_i}{\partial x_j}\right)\left(\frac{\partial v_i}{\partial x_j}\right), \tag{4.9}$$

[2] $\mathrm{TE}(r)$ is usually called the temperature variance, but we reserve the term "variance" for another quantity.

where the first term on the right-hand side of equation (4.9) is KE_{in}, the total rate at which kinetic energy is pumped into the fluid from buoyancy forces, and the second term on the right-hand side is KE_{out}, a negative-definite quantity that is the rate at which viscosity dissipates the kinetic energy. If the convective flux is much greater than the conductive flux and if the time variation of $\langle T \rangle$ is slow enough that

$$\langle TV_r \rangle \approx \mathscr{L}/r^2 , \tag{4.10}$$

then

$$\mathscr{L}(r) \gg \left| \partial \left(\int_0^r dr' r'^2 \langle T \rangle \right) \Big/ \partial t \right| \tag{4.11}$$

and

$$KE_{in} \approx 4\pi PrRs \int_0^1 \mathscr{L}(r) r dr = 1.892\pi PrRs . \tag{4.12}$$

In dimensionless units the rate at which mean thermal energy is generated is unity. From equation (4.12) it is apparent that in Boussinesq fluids the rate at which kinetic energy is created is much greater than the rate at which the mean thermal energy is created. This conclusion is quite different from the one derived from mixing-length arguments in a compressible fluid. In a compressible fluid these two energy input rates are nearly the same. It is because a Boussinesq fluid is incompressible (and can perform no mechanical work) that the mean thermal energy generation rate and kinetic energy generation rate are not equipartitioned.

It is often assumed that the rate at which kinetic energy enters the fluid is approximately equal to V_{big}^3/L_{big}, where V_{big} and L_{big} are the characteristic velocity and length of the largest convective eddies. Equating this expression for KE_{in} with equation (4.12), we obtain

$$V_{big} \approx (PrRs)^{1/3} . \tag{4.13}$$

This provides a scaling law for V_{big} that can be numerically verified. Furthermore, if most of the convective flux is transported by the largest convective eddy (with characteristic temperature fluctuation $\sim T_{big}$), then

$$\langle \tilde{T}_{big} V_{big} \rangle \approx \mathscr{L}/r^2 \approx 1 \tag{4.14}$$

and

$$T_{big} \approx (PrRs)^{-1/3} . \tag{4.15}$$

Equation (4.13) can also be verified numerically.

By multiplying the thermal diffusion equation by $\tilde{T}$ and integrating over the volume, we obtain the fluctuating thermal energy budget

$$\partial \left[\frac{1}{2} \int dr^3 \langle \tilde{T}^2 \rangle \right] \Big/ \partial t = -4\pi \int_0^1 \langle \tilde{T} v_r \rangle \frac{\partial \langle T \rangle}{\partial r} r^2 dr - 4\pi \int_0^1 \langle \nabla \tilde{T} \cdot \nabla \tilde{T} \rangle r^2 dr . \tag{4.16}$$

The first term on the right-hand side of equation (4.16) is TE_{in}, the rate at which fluctuating thermal energy is created from the interaction of the mean temperature gradient with the convective flux. The second term on the right-hand side of equation (4.14) is TE_{out}, a negative definite quantity that is the rate of diffusion of the thermal energy.

d) Detailed Energy Budgets for Each l-Value

Each shell of modes with the same horizontal wavelength [i.e., all modes (γ, l, m) with the same value of l] has an inflow and outflow of kinetic and fluctuating thermal energy. It is useful to determine the rate at which energy is dissipated and created in each particular l-shell. The rate of change of the kinetic energy in the lth shell is

$$\partial \left[4\pi \int_0^1 KE(r, l) r^2 dr \right] \Big/ \partial t = KE_{in}(l) - KE_{out}(l) - 4\pi \int_0^1 \langle \boldsymbol{v}(r, l) \cdot [(\boldsymbol{v} \cdot \nabla) \boldsymbol{v}] \rangle r^2 dr , \tag{4.17}$$

where $KE_{in}(l)$ is equal to the rate at which kinetic energy is directly fed into the lth shell:

$$KE_{in}(l) = 4\pi PrRs \sum_{\gamma,m} l(l+1) \int_0^1 \omega_{\gamma,l,m} T_{\gamma,l,m} r^2 dr , \tag{4.18}$$

and where $KE_{out}(l)$ is the rate at which the lth shell directly loses kinetic energy through viscous dissipation:

$$KE_{out}(l) = -4\pi Pr \int_0^1 \left[\left[r^{-1} \partial^2 [r\, KE\,(l, r)]/\partial r^2 + \sum_{\gamma,m} \left\{ -[l(l+1)]^2 r^{-2} \omega_{\gamma,l,m} \mathscr{D}_l(\omega_{\gamma,l,m}) \right. \right. \right.$$
$$\left. \left. \left. - l(l+1) r^{-2} \frac{\partial (r\omega_{\gamma,l,m})}{\partial r} \partial [r \mathscr{D}_l(\omega_{\gamma,l,m})]/\partial r - l(l+1) \psi_{\gamma,l,m} \mathscr{D}_l(\psi_{\gamma,l,m}) \right\} \right] \right] r^2 dr . \tag{4.19}$$

In equation (4.17), $\boldsymbol{v}(r, l)$ is the velocity associated with the lth shell at radius r. If the flow is stationary, the left-hand side of equation (4.17) is zero, but $\langle\langle \mathrm{KE}_{\mathrm{in}}(l)\rangle\rangle \neq \langle\langle \mathrm{KE}_{\mathrm{out}}(l)\rangle\rangle$ because $-4\pi \int \langle \boldsymbol{v}(r, l)\cdot[(\boldsymbol{v}\cdot\nabla)\boldsymbol{v}]\rangle r^2 dr$, which is the rate at which kinetic energy cascades in or out of the lth shell from other shells, it is not necessarily zero. By comparing the relative values of $\mathrm{KE}_{\mathrm{in}}(l)$, $\mathrm{KE}_{\mathrm{out}}(l)$, and $-4\pi \int \langle \boldsymbol{v}(r, l)\cdot[(\boldsymbol{v}\cdot\nabla)\boldsymbol{v}]\rangle r^2 dr$, we can determine whether an l-shell is part of the production, dissipation, or equilibrium range of the spectrum.

The rate of change of fluctuating thermal energy in the lth shell is given by

$$\partial\left[4\pi \int_0^1 \mathrm{TE}(r, l) r^2 dr\right] \Big/ \partial t = \mathrm{TE}_{\mathrm{in}}(l) - \mathrm{TE}_{\mathrm{out}}(l) - 4\pi \int_0^1 \langle T(l, r)[(\boldsymbol{v}\cdot\nabla)\tilde{T}]\rangle r^2 dr \,. \tag{4.20}$$

The rate of fluctuating thermal energy input, $\mathrm{TE}_{\mathrm{in}}(l)$, is

$$\mathrm{TE}_{\mathrm{in}}(l) = -4\pi \int_0^1 \frac{\partial\langle T\rangle}{\partial r} r \sum_{\gamma,m} T_{\gamma,l,m}\omega_{\gamma,l,m} l(l+1) dr \,, \tag{4.21}$$

and the rate of fluctuating thermal energy dissipation is

$$\mathrm{TE}_{\mathrm{out}}(l) = -4\pi \sum_{\gamma,m} [(\partial T_{\gamma,l,m}/\partial r)^2 + l(l+1) r^{-2} T_{\gamma,l,m}{}^2] r^2 dr \,. \tag{4.22}$$

The rate at which fluctuating thermal energy cascades in or out of the lth shell from neighboring shells is

$$-4\pi \int_0^1 T(l, r)[(\boldsymbol{v}\cdot\nabla)\tilde{T}] r^2 dr \,,$$

where $T(l, r)$ is the thermal fluctuation of the lth shell at radius r.

e) *Vorticity, Isotropy, and Angular Momentum*

The vorticity $\mathscr{R}$ is solenoidal and can be expressed in terms of modes as

$$\mathscr{R} = \nabla[\partial(r\psi)/\partial r] - (r\nabla^2\psi)\hat{e}_r - r\nabla[(\nabla^2\omega)\hat{e}_r] \,. \tag{4.23}$$

One possible test for the isotropy of the velocity is to compute the helicity, $\langle \mathscr{R}\cdot\boldsymbol{v}\rangle$, which is zero for an isotropic field. In terms of modes, the helicity is given by

$$\langle \boldsymbol{v}\cdot\mathscr{R}\rangle = l(l+1) r^{-2} \sum_{\gamma,l,m} 2l(l+1)\omega_{\gamma,l,m}\psi_{\gamma,l,m} + \frac{\partial(r\omega_{\gamma,l,m})}{\partial r}\frac{\partial(r\psi_{\gamma,l,m})}{\partial r} - r\psi_{\gamma,l,m}\frac{\partial^2(r\omega_{\gamma,l,m})}{\partial r^2} \,. \tag{4.24}$$

From equation (4.24) it is clear that the helicity is made up of terms that are proportional to $\psi_{\gamma,l,m}\omega_{\gamma,l,m}$ and its derivatives. We normally expect that the poloidal part of the velocity is dominated by the low l modes, whereas the toroidal component of the velocity (as well as the vorticity itself) is dominated by the high l modes. Therefore the helicity is less a test of isotropy than a measure of the correlation between the large scale and small structure of the velocity. In a calculation where the large scale communicates with the small scale by a series of cascades (each of which introduces its own phase shifts), the helicity is not a useful measure of isotropy. Instead, we shall use a less rigorous but more straightforward and revealing method to determine the anisotropy of the velocity. We define an isotropy function, $I(l, r)$ as a function of r for each l-shell to be

$$I(l, r) = \tfrac{1}{2}\mathrm{KE}_{\mathrm{H}}(l, r)/\mathrm{KE}_{\mathrm{R}}(l, r) \,, \tag{4.25}$$

where $\mathrm{KE}_{\mathrm{R}}(l, r)$ and $\mathrm{KE}_{\mathrm{H}}(l, r)$ are the contributions to the kinetic energy, $\mathrm{KE}(l, r)$, that are due respectively to the radial and horizontal components of the velocity. If $I(l, r) = 1$, the flow is defined as isotropic. There are several advantages in defining a measure of isotropy as a function of both l and r. First of all, convection is not by nature isotropic; the buoyancy force is in the radial direction, so we expect the radial component of the velocity to dominate. We expect that $I(l, r)$ will be less than 1 when l is part of the production range. For larger l-shells we expect that the velocity field will no longer feel the direct effect of the radial buoyancy; as the energy cascades downward, the velocity should lose its memory of the radial direction and become more isotropic. This return to isotropy can be tested by determining whether $I(l, r)$ increases with increasing l. We also expect $I(l, r)$ to vary with the radius. At the outer boundary of the sphere, the radial component of the velocity goes to zero. The outer boundary layer should be characterized by large values of $I(l, r)$. We determine the behavior of $I(l, r)$ by expressing it in terms of modes:

$$I(l, r) = \sum_{\gamma,m} l(l+1)\omega_{\gamma,l,m}{}^2 \Big/ \sum_{\gamma,m} \{[\partial(r\omega_{\gamma,l,m})/\partial r]^2 + r^2\psi_{\gamma,l,m}{}^2\} \,. \tag{4.26}$$

By using the regularity conditions at the origin, equation (4.26) shows that

$$\lim_{r\to 0} I(l, r) \to 1 \quad \text{for all } l\,. \tag{4.27}$$

Equation (4.27) is due to the singularity of the coordinate system at the origin (i.e., there is no distinction between radial and horizontal), so $I(l, r)$ is not a useful measure of isotropy at the origin. (However, at the origin $I(l, r)$ is the ratio of two small, numerically computed quantities. By comparing it to its known analytic behavior at the origin, it provides us with a useful test of the accuracy of our numerical code.)

One more useful quantity to compute is the distribution of angular momentum in the fluid. All of the angular momentum resides in the $l = 1$ toroidal modes. Defining $\boldsymbol{j}(r)$ to be the angular momentum per unit mass at radius r, we find (Paper I):

$$\boldsymbol{j}(r) = 2(3)^{-1/2} r(\psi_{R,1,0}\hat{e}_z - \psi_{R,1,0}\hat{e}_x - \psi_{I,1,1}\hat{e}_y)\,. \tag{4.28}$$

V. RESULTS OF NUMERICAL CALCULATIONS FOR RAYLEIGH NUMBER = 10^4 AND PRANDTL NUMBER = 10

a) Convergence to a Unique Stable, Equilibrium Solution

We have integrated the artificial and real time equations for $\mathrm{Rs} = 10^4 (\sim 33.8\mathrm{Rs}_{\mathrm{crit}})$ and $\mathrm{Pr} = 10$, using a code that is second-order accurate in both space and time. The solution to the artificial time equations was found to be time-independent. This solution, plus a perturbation, was used as the initial data in the real time equations. The perturbation decayed, and the solution reconverged to the steady-state solution of the artificial time equations. We performed the integration several times: we used a radial grid that varied between 64 and 128 zones, and l_{cutoff} in the Galerkin truncation that varied between 6 and 12, several different time steps, and a large number of different initial conditions to the artificial and real time equations. (All of the initial conditions had total angular momentum equal to zero.) In each case the integrations converged to the same time-independent solution. (When l_{cutoff} was less than 12, we found that the small l modes did not change, but there was some change in the modes with l near l_{cutoff}. (See § V*c*.)

The final, stable solution has two orthogonal planes of reflection symmetry. Despite our attempts to introduce perturbations without this symmetry, the solution stubbornly remained reflection symmetric. Modes with other symmetries, such as dodecahedral modes, were found to be unstable.

A solution that is reflection symmetric with respect to both the $x = 0$ plane and $z = 0$ plane can be written so that ω and T are made up only of (R, l = even, m = even) and (I, l = odd, m = odd) modes and ψ made up only of (R, l = even, m = odd) and (I, l = odd, m = even) modes. However, in no case did the planes of symmetry coincide with the $x = 0$, $y = 0$, or $z = 0$ planes; therefore, *all* modes are present in our final solutions. In fact, different initial conditions always lead to different final values of $\omega_{\gamma,l,m}$, $\psi_{\gamma,l,m}$, $T_{\gamma,l,m}$, $P_{\gamma,l,m}$, and $\Phi_{\gamma,l,m}$ because the planes of symmetry always lie in different directions. We consider it an excellent test of our numerical code (especially the cumbersome nonlinear terms) that all of the different initial conditions lead to solutions with different planes of symmetry and that the solutions are identical whey they are rotated such that their planes of symmetry coincided with the $x = 0$ and $y = 0$ planes.

Notice that a solution with two orthogonal planes of reflection symmetry has its angular momentum identically equal to zero in all of its radial shells; if the solution is oriented such that the planes of reflection lie in the $x = 0$ planes, then $\psi_{R,l=1,m=1} = \psi_{R,l=\Phi,m=0} = \psi_{I,l=1,m=1} = 0$; therefore, $\boldsymbol{j}(r) = 0$ for all r. Conservation of angular momentum requires only the integral constraint

$$\int_0^1 \boldsymbol{j}(r) r^2 dr = 0\,.$$

The system was not constrained to have $\boldsymbol{j}(r) = 0$ for all r. We also note that although the $l = 1$ component of the toroidal component of the velocity vanishes identically, the toroidal velocity is about one-tenth the poloidal velocity for $l = 2$.

b) Temperature Gradient and Heat Flux

The mean temperature gradient of the steady-state convective solution is shown in Figure 1 (solid line) along with the temperature gradient of the conductive solution (*dotted line*). The convective gradient is, of course, more isothermal than the conductive solution, but it still shows a cusp at $r = 0.3$, which is the boundary of the internal heat source. Apparently the convective velocity and temperature fluctuations are sufficiently local that the convective flux cannot completely smooth out the cusp at $r = 0.3$. Because the convective solution is steady state, $(1/r)\partial\langle T\rangle/\partial r$ must be equal to -1 at the outer boundary. The slope of $(1/r)\partial\langle T\rangle/\partial r$ must be equal to zero at the origin. The temperature gradient is positive between $r = 0.55$ and $r = 0.86$, which means that the convective flux is so large that the conductive flux is negative in this region. A negative conductive flux is a familiar property of

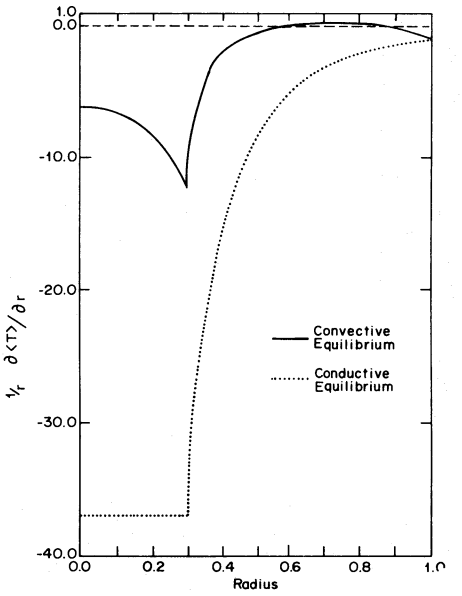

FIG. 1.—The mean temperature gradients for conductive equilibrium (*dotted line*) and convective equilibrium (*solid line*) as a function of radius. The derivatives of both gradients are discontinuous at $r = 0.3$, the outer boundary of the heat source. The convective gradient is nearly isothermal outside of $r = 0.3$ and is positive for $0.55 < r < 0.86$.

convection in plane-parallel geometries (Herring 1963). Figure 2 shows the ratio $F_{\rm con}/F_{\rm total}$, where $F_{\rm total}$ is the total flux and is equal to $\mathscr{L}(r)/r^2$ in steady-state convection. The ratio $F_{\rm con}/F_{\rm total}$ is the ratio of heat flux that is carried by convection to the total heat flux. The ratio is near unity over most of the radius of the sphere except in the outer boundary layer where it must go to zero. In § IV it was shown that the slope of $F_{\rm con}/F_{\rm total}$ goes to zero at the origin (unless the leading order terms of $\omega_{\gamma,l=1,m}$ or $\tilde{T}_{\gamma,l=1,m}$ vanish at the origin). The mean temperature as a function of radius (Fig. 3) prominently shows a "footprint" of the $r = 0.3$ boundary. Boundary conditions necessitate that $\langle T(1)\rangle$ be zero for both the convective and conductive solution, but the value of $\langle T\rangle$ at the origin can change. In conductive equilibrium $\langle T(0)\rangle = 4.0$, whereas in convective equilibrium $\langle T(0)\rangle = 0.68$.

c) *Energy Spectra*

The two-dimensional spectra of the kinetic and fluctuating thermal energies evaluated at $r = 0.5$ are shown in Figure 4 and 5. Both curves clearly exhibit the exponential decay that is characteristic of a dissipation spectrum. The total rate at which kinetic energy is dissipated from the fluid, $\mathrm{KE}_{\rm out}$, is determined from equation (4.22) and is found to be 4.96×10^5. The Kolmogorov length scale, η, is defined (Tennekes and Lumley 1972) as

$$\eta \equiv (\mathrm{Pr}^3/\langle\langle \mathrm{KE}_{\rm out}\rangle\rangle)^{1/4}, \tag{5.1}$$

and is equal to 0.212 in dimensionless units.

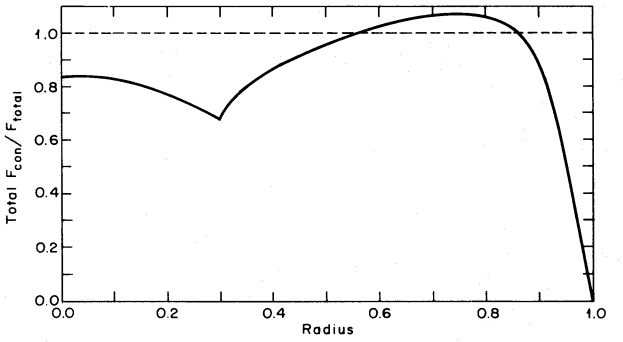

FIG. 2.—The ratio of the convective heat flux to the total (convective and conductive) flux. For $0.55 < r < 8.6$, the ratio is greater than 1, which means that conduction carries energy *downward* in this region.

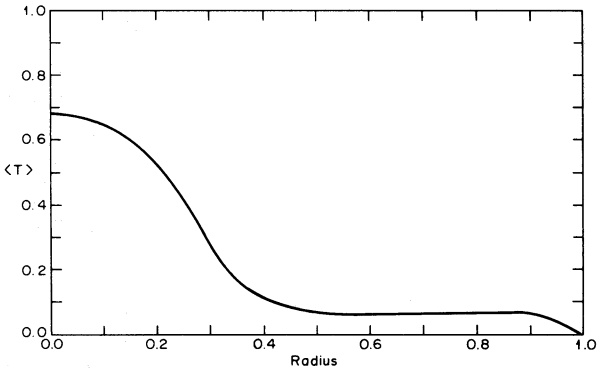

FIG. 3.—The mean temperatures of the convecting fluid as a function of radius. The temperature of $r = 1$ is zero due to boundary conditions. The central temperature is free to vary, and the convective flux has reduced it from its value of 4.0 in conductive equilibrium to 0.68 in convective equilibrium. The boundary layer at $r \approx 0.88$ and the boundary of the heat source at $r = 0.3$ are apparent.

The equivalent thermal length-scale, η_θ, for which thermal diffusion becomes overwhelming is defined as

$$\eta_\theta = \mathrm{Pr}^{-1/2}\eta\,, \tag{5.2}$$

and is equal to 0.067. With 128 grid points and $l_{\mathrm{cutoff}} = 12$, both of these scales should be numerically resolvable. Because η is greater than η_θ, we expect the dissipation part of the kinetic energy spectrum to extend to lower values of l than in the fluctuating temperature spectrum. Nearly the entire kinetic energy spectrum is exponential while $\mathrm{TE}(l, r = 0.5)$ is fairly flat for $l \leq 3$. This flatness is due to the combined effects of production, cascade, and dissipation. Because all of the effects are squeezed into a short range of the spectrum, there is no clearly identifiable production or convective-viscous subrange. For $l > 3$, $\mathrm{T3}(l, r)$ is dominated by dissipation.

Both $\mathrm{TE}(l, r)$ and $\mathrm{KE}(l, r)$ curl upward at the high-l end of the spectrum. This is a typical phenomenon of a Galerkin truncation and is due to the fact that energy can cascade down the spectrum until it reaches l_{cutoff}. At l_{cutoff} the energy can cascade no further, so the velocity at l_{cutoff} is forced to increase until $\mathrm{KE}_{\mathrm{out}}(l_{\mathrm{cutoff}})$ is large enough to dissipate all of the accumulated energy. The fact that $\mathrm{TE}(l, r)$ curls up more than $\mathrm{KE}(l, r)$ is due to the fact that $\mathrm{Pr} > 1$. Most of the kinetic energy can dissipate before cascading into l_{cutoff}. However, the fluctuating thermal energy is not dissipated as efficiently, so more cascades down to l_{cutoff} before being dissipated, resulting in a greater curl. We have shown that the upward curl at l_{cutoff} is a truncation effect by repeating the calculation with $l_{\mathrm{cutoff}} = 10$. In the latter calculation the spectra curl at $l = 10$ while with $l_{\mathrm{cutoff}} = 12$ there was no curl at $l = 10$. If the integration is performed with a Prandtl number of 0.1, $\mathrm{KE}(l, r)$ curls up more than $\mathrm{TE}(l, r)$.

It is because $\mathrm{TE}(l, r)$ and $\mathrm{KE}(l, r)$ both decay exponentially at large l that our modal truncation is valid. If we found that $\mathrm{KE}(l, r)$ or $\mathrm{TE}(l, r)$ decayed slowly as a function of l, the modal truncation would not have been a good approximation.

We have computed the kinetic energy spectrum as a function of the three-dimensional wavenumber k, using the formulae in the Appendix. According to Corrsin (1964) the three-dimensional dissipative kinetic energy spectrum

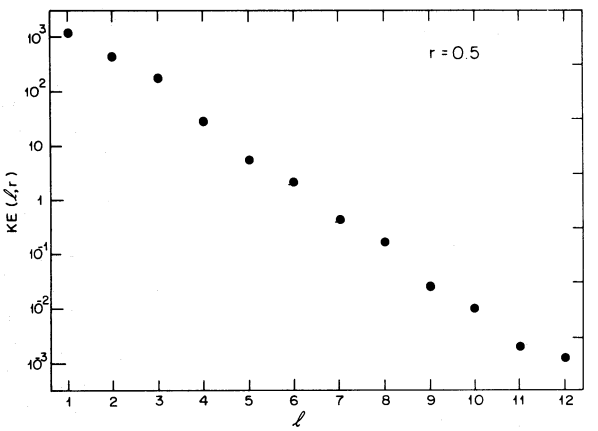

FIG. 4.—The kinetic energy spectrum at $r = 0.5$ for Reynolds number ~ 3 as a function of l. The spectra show a nearly exponential decay with no trace of a production or equilibrium range. The slight curl upward at $l = 12$ is due to truncation.

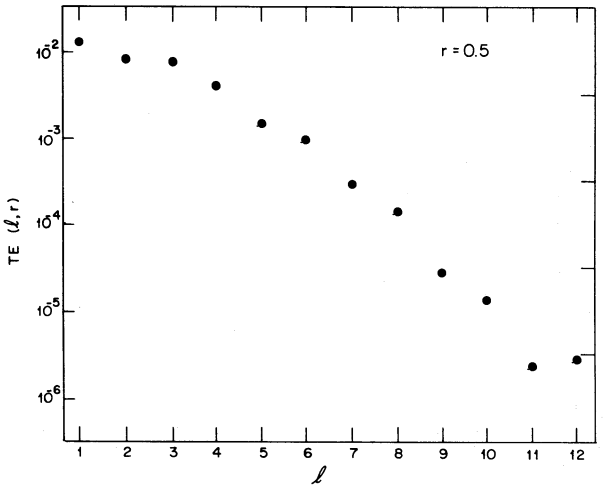

FIG. 5.—The thermal energy spectrum at $r = 0.5$ as a function of l for a Peclet number of ~ 34. The thermal spectrum falls off less steeply than the corresponding kinetic energy spectrum. The flatness of the spectrum at $l \leq 3$ is due to a combination of production and cascade of thermal energy. The upward curl at $l = 12$ due to truncation is more severe in this figure than it is in Fig. 4 for the kinetic energy.

should be of the form

$$\mathrm{KE}(k) = \alpha \epsilon^{2/3} k^{-5/3} \exp\left[-3\alpha(k\eta)^{4/3}/2\right], \tag{5.3}$$

where α is a constant on the order of unity. Figure 6 shows our computed spectrum with $(k\eta)^{4/3}$ as the independent variable. Fitting the slope of the curve in Figure 6 to equation (5.3) between $k = 4$ and $k = 8$, we have determined α to be 3.07.

Recently, other expressions for the three-dimensional energy spectrum in the dissipative range have been derived using closure methods which show that

$$\mathrm{KE}(k) \sim k^{\beta} \exp(-k\eta), \tag{5.4}$$

where the exponent β depends on the exact form of the closure. With less than a decade of range in k, we are unable to differentiate between equations (5.3) and (5.4) for the correct form of KE(k).

Since both TE(l, r) and KE(l, r) decay exponentially with l, it is not surprising that the convective flux, $\sim F_{\mathrm{con}}(l)$, carried by the lth shell of modes, decreases with l. Figure 7 shows the fraction of the convective flux carried by the lth shell at $r = 0.5$. Nearly 90% of the convective flux is carried by the $l = 1$ modes. We conclude that the amount of flux we have neglected by truncating at $l = 12$ is negligible.

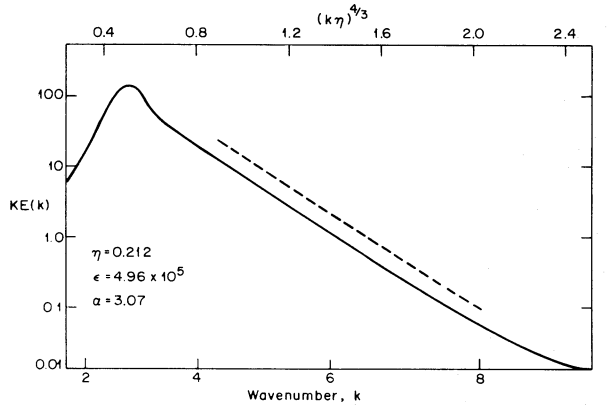

FIG. 6.—The kinetic energy spectrum as a function of $(k\eta)^{4/3}$, where k is the three-dimensional wavenumber and η is the Kolmogorov length. By fitting the slope of this calculated curve for $4.0 \leq r \leq 8.0$ to the theoretical dissipation spectrum $KE(k) \propto \exp\left[-3\alpha(k\eta)^{4/3}/2\right]$, we have computed the dimensionless constant α to be 3.07.

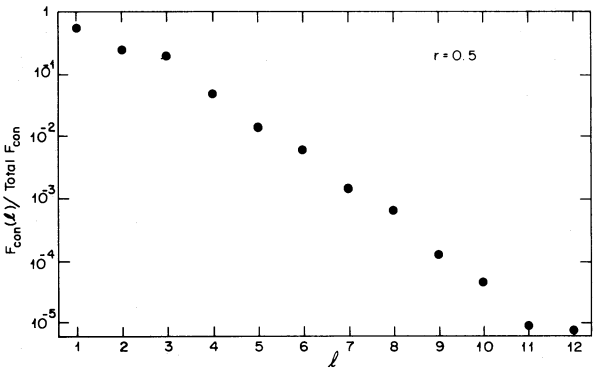

FIG. 7.—The fraction of the convective flux at $r = 0.5$ carried by all modes with horizontal wavenumber l is plotted as a function of l. Nearly 90% of the convection flux is carried by the $l = 1$ mode. Like the thermal and kinetic energy spectra, the convective flux decreases exponentially with increasing l.

d) Energy Balance

In Figure 8 we have plotted $TE_{in}(l)/TE_{in}$ and $KE_{in}(l)/KE_{in}$ which are, respectively, the fractions of thermal and kinetic energy that each l-shell contributes to the fluid. These ratios both decrease rapidly as l increases, with ~93% of KE_{in} and ~73% of TE_{in} produced by the $l = 1$ modes. Because the Prandtl number is greater than 1, $KE_{in}(l = 1)/KE_{in}$ is greater than $TE_{in}(l = 1)/TE_{in}$. Furthermore, $KE_{in}(l)/KE_{in}$ decreases faster than $TE_{in}(l)/TE_{in}$.

We have plotted the ratios $KE_{out}(l)/KE_{in}(l)$ and $TE_{out}(l)/TE_{in}(l)$ in Figure 9. The ratio $KE_{out}(l)/KE_{in}(l)$ is equal to the rate at which kinetic energy is directly dissipated (not leaked through a cascade) from the lth shell divided by the rate at which kinetic energy directly enters the lth shell. We would expect this ratio to be small if l were in a production range and to be large if it were in the dissipative range. The fact that $KE_{out}(l)/KE_{in}(l)$ is approximately 1 for all l can be interpreted in the following way: there is no (or very little) kinetic energy cascade, so the amount of kinetic energy that is generated in the lth shell is directly dissipated by the lth shell and not transferred to neighboring shells. This interpretation is supported by the fact that the computed nonlinear terms in the model Navier-Stokes equation (2.7) are much smaller than the viscous pressure and buoyancy terms. The lack of nonlinear interaction is also shown by the fact that the poloidal velocity (which is directly fed by buoyancy) is much larger than the toroidal velocity, which is fed energy only through the nonlinear cascade. The values of $TE_{out}(l)/TE_{in}(l)$ plotted in Figure 9 show that there is a thermal cascade. $TE_{out}(l)TE_{in}(l)$ is less than 1, which means some of the fluctuating thermal energy in the $l = 1$ shell must be cascading to higher values of l. For $l \geq 2$, $TE_{out}(l)/TE_{in}(l)$ is larger than 1, which means these modes are dissipating more energy than they produce. The extra energy that these shells dissipate is provided by their neighbors. The thermal cascade is plausible because the nonlinear terms of the thermal diffusion equation (2.9) are of the same order as the dissipative terms.

A test of the accuracy of our code is that it conserves energy; the computed values of KE_{out} and KE_{in} are 4.96×10^5 and 4.94×10^5, respectively. The computed values of TE_{out} and TE_{in} are 4.09 and 4.08.

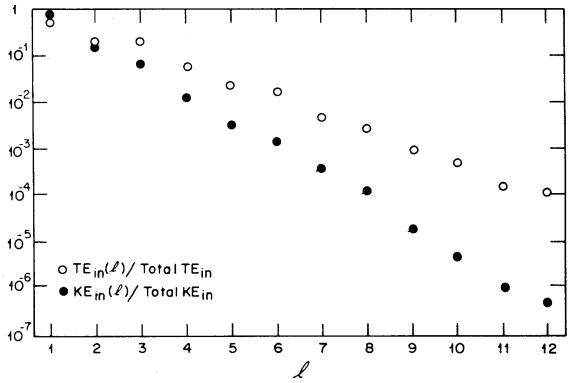

FIG. 8.—The fraction of the total amount of kinetic (thermal) energy that is produced in the lth shell of modes is shown by the solid (open) circles. While 93% of the kinetic energy is produced by the $l = 1$ mode, only 73% of the thermal energy is produced by that mode. The figure shows that the production of thermal energy is more important than the production of kinetic energy in high l-shells.

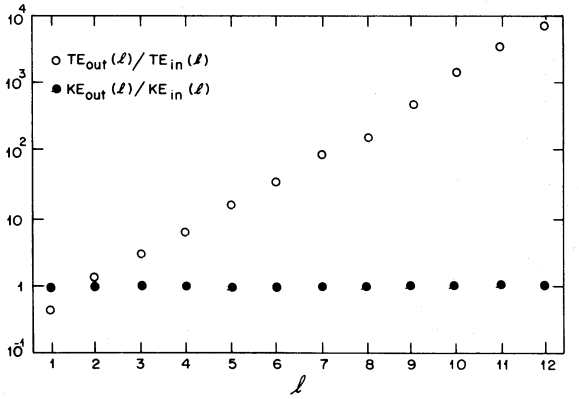

FIG. 9.—The ratio of the kinetic (thermal) energy that is viscously dissipated by the lth shell of modes divided by the amount of kinetic (thermal) energy that is produced in the lth shell is plotted as solid (open) circles. The ratio for the kinetic energy is near unity for all l and is indicative of no kinetic energy cascade; all of the kinetic energy produced in the lth shell is dissipated there before it has a chance to cascade to a different l shell. For $l = 1$ the ratio for the thermal energy shows that more energy is produced there than dissipated; this indicates that thermal energy escapes from the $l = 1$ shell by cascading into higher l shells. For $l \geq 2$ the thermal ratio is greater than 1 and increases exponentially, indicating that the lth shell dissipates more thermal energy than it produces. The extra energy that is dissipated is provided by the energy cascade.

e) Structure of the $l = 1$ Modes

Because the $l = 1$ modes dominate the flow, we illustrate the $l = 1$ radial component of the velocity, $l(l + 1)r^{-1}\omega_{l,1,1}$ in Figure 10 and the temperature, $\tilde{T}_{l,1,1}$, in Figure 11. The $l = 1$ component of the toroidal velocity, ψ, is equal to zero for all r. For these two figures, we have rotated the planes of symmetry to coincide with the $x = 0$ and $z = 0$ plane. Figure 10 is normalized by the maximum value of the $l = 1$ radial component of the velocity, $\max v_r^{l=1} = 33.8$. Notice that the velocity is a smooth function of radius and shows no cusp at $r = 0.3$. On the other hand, $\tilde{T}_{l,1,1}$ does show a strong peak at $r = 0.3$. Figure 11 is normalized by its maximum value, $\max T_{l,1,1} = 0.0226$. It is interesting to compare the maximum value of $v_r^{l=1}$ with its estimated value of 46 derived from the scaling law (eq. [4.28]). The scaling law for the velocity is therefore fairly accurate for this flow. The Peclet number, in dimensionless units, is just equal to the velocity, so the Reynolds number is approximately equal to $\max v_r^{l=1}/\mathrm{Pr} \approx 3$.

f) The Two-Dimensional Spectra and Boundary Layer Thickness

In Figures 12 and 13 we have plotted $\mathrm{KE}(l, r)/r^2$ and $\mathrm{TE}(l, r)/r^2$ as functions of radius for all l. All of the 24 graphs have been normalized by their maximum values. Except for $l = 1$, $\mathrm{KE}(l, r)/r^2$ is zero at the origin. As r increases, the curves remain near zero until they reach a critical value of radius and steeply rise to a peak. The critical value of r at which the curves begin to rise and the radius of the peak itself both increase with increasing values of l. This behavior is consistent with the fact that $\mathrm{KE}(l, r) \sim r^{2l}$ near the origin (Paper I). For $l \geq 2$, $\mathrm{KE}(l, r)/r^2$ decreases after its peak to a local minimum and then sharply increases at $r = 1.0$. This is because most of the kinetic energy in the first peak is due to radial motions. As v_r goes to zero at $r = 1$, $\mathrm{KE}(l, r)/r^2$ decreases. Very close to the outer boundary, the horizontal components of the velocity increase rapidly in order to conserve mass flux, and $\mathrm{KE}(l, r)/r^2$ increases accordingly.

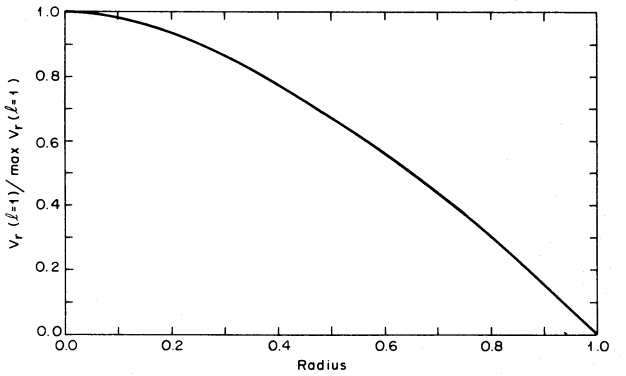

FIG. 10.—The radial component of the $l = 1$ velocity as a function of radius. The velocity has been normalized by its maximum value of 33.8. The velocity shows no trace of the boundary of the heat source at $r = 0.3$.

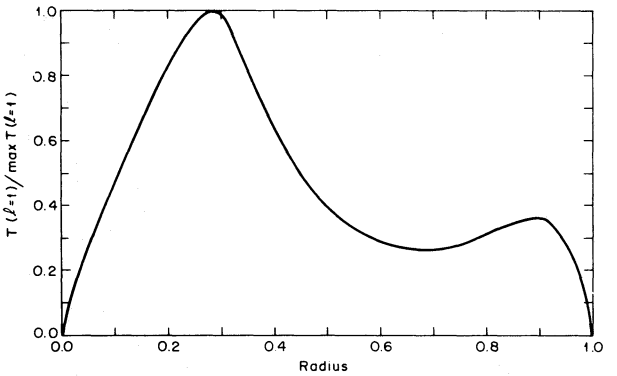

FIG. 11.—The $l = 1$ component of the temperature as a function of radius. The temperature is normalized by its maximum value of 0.0226. The temperature has an obvious peak at the boundary of the heat source.

We define $\chi(l)$ to be the distance between $r = 1.0$ and the radius of the local minimum of $\mathrm{KE}(l, r)/r^2$, and we use it as a measure of the boundary-layer thickness for each l. Figure 12 shows that for $l \leq 6$, $\chi(l)$ slowly decreases with increasing l, and remains at a nearly constant value for $l \geq 7$. The values of $\chi(l)$ were found to be insensitive to changes in the number of radial grid points or to stretching the grid near the boundary. We can understand the behavior of $\chi(l)$ by examining the energetics of the boundary layer. The rate at which kinetic energy is dissipated from the boundary-layer associated with the lth shell is

$$4\pi \mathrm{Pr} \int_{1-\chi}^{1} \boldsymbol{v}(l, r) \cdot \nabla^2 \boldsymbol{v}(l, r) r^2 dr \approx 4\pi \mathrm{Pr} v(l, r = 1)^2 / \chi \,. \tag{5.5}$$

What is the rate at which kinetic energy enters the boundary layer? For large values of l, the amount of kinetic energy that enters the boundary layer directly from the buoyancy forces is small compared to the rate at which kinetic energy is advected in. The rate of advection is proportional to the density of kinetic energy in the lth shell multiplied by the surface area of the boundary layer ($\sim 4\pi$) multiplied by the largest characteristic velocity, V_{big}:

$$2\pi [v(l, r = 1)]^2 V_{\mathrm{big}} \,. \tag{5.6}$$

Setting expressions (5.5) and (5.6) equal to each other, we see that $v(l, r = 1)$ cancels and that $\chi(l)$ becomes independent of $v(l, r)$ and l for large l.

The thermal energy spectra, $\mathrm{TE}(l, r)$, display some of the same properties that the kinetic energy spectra have. As l increases, the radius at which the spectra rise and peak also increases. This is not surprising since both $\mathrm{TE}(l, r)$ and

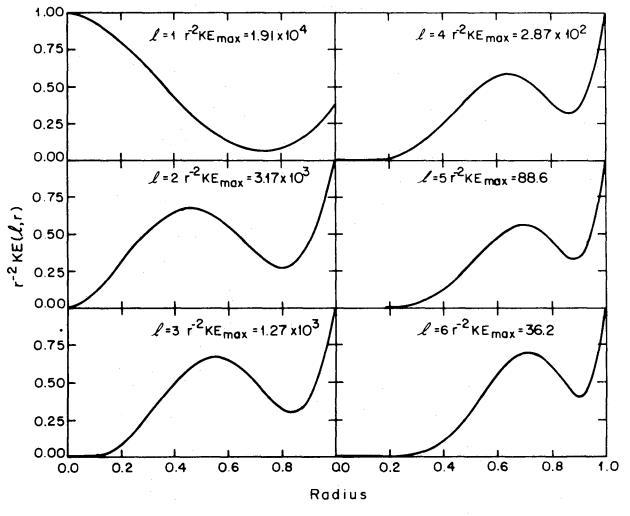

FIG. 12a

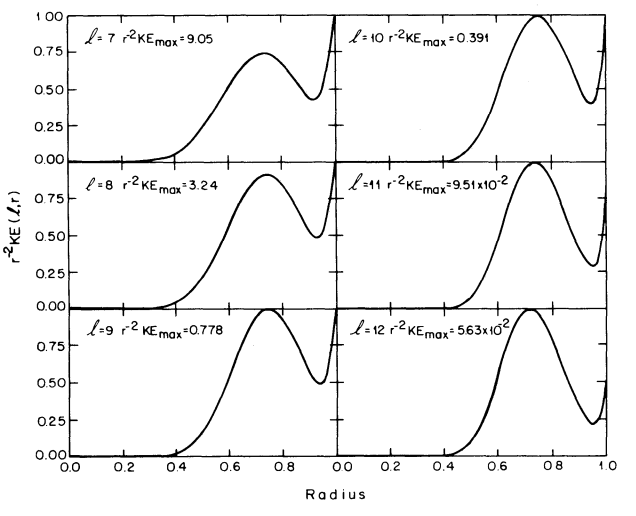

FIG. 12b

FIG. 12.—The kinetic energy spectra $\mathrm{KE}(l, r)/r^2$ as functions of radius for $l = 1$, 12. As l increases, the spectra peak at increasing values of the radius. The edge of the outer boundary layer is approximately equal to the radius of the local minimum of $\mathrm{KE}(l, r)/r^2$ near $r = 1.0$. For $1 < l \leq 6$ the thickness of the layer decreases slowly with increasing l. For $l > 6$ the thickness is nearly constant.

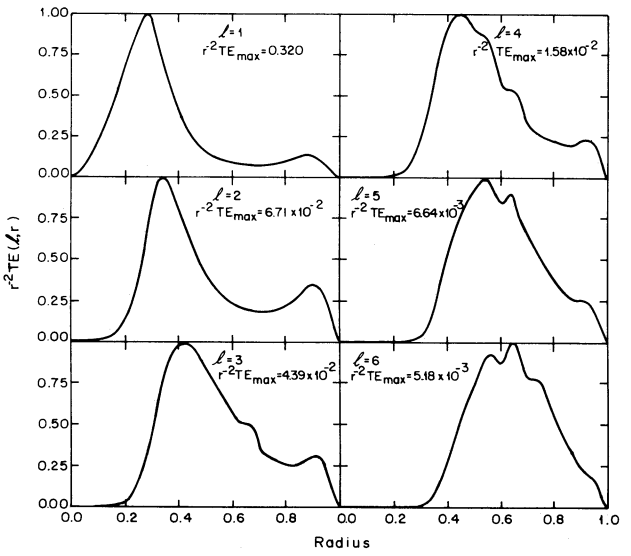

FIG. 13*a*

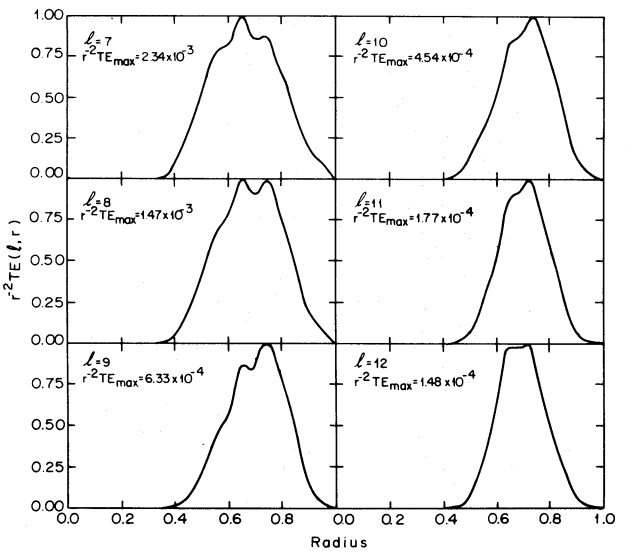

FIG. 13*b*

FIG. 13.—The thermal energy spectra $TE(l, r)/r^2$ as a function of radius. As l increases, the radii of the maximum values of these spectra increase. For $l < 6$ there is a secondary peak near the edge of the boundary layer. At $l = 6$ the two peaks merge, and for higher l only one peak can be seen. There is more radial structure in the thermal than in the kinetic energy spectra because the thermal fluctuation are less easily dissipated when the Prandtl number is greater than 1.

$KE(l, r)$ behave as r^{2l} near the origin. Unlike the kinetic energy spectra, though, $TE(l, r)/r^2$ shows several peaks. For $TE(l = 1, r)/r^2$ (the square of the function plotted in Fig. 11) a large peak occurs at the boundary of the heat source, $r = 0.3$, and a smaller peak occurs at $\sim r = 0.88$, the radius at which the convective flux (Fig. 2) drops to zero. These two peaks can be seen in $TE(l, r)/r^2$ for $l < 6$. At $l = 6$ the two peaks merge. Comparing Figures 12 and 13, it is strikingly apparent that $TE(l, r)/r^2$ has a more small-scale structure than $KE(l, r)/r^2$. At first this structure was thought to be numerical. Testing shows that it is reproducible and independent of radial grid changes. One reason that the kinetic energy is smoother than the thermal energy spectrum is that the Prandtl number is greater than 1. Viscosity is better at smoothing the velocity than thermal diffusivity is at smoothing the temperature. As further evidence of the viscosity's smoothing effect, we have seen (Fig. 10) that the $l = 1$ component of the velocity shows no evidence of the heat source, while the temperature shows a marked peak. The small-scale radial structure in $T_{\gamma,l,m}$ is due to the temperature and momentum advection terms, $(\boldsymbol{v}\cdot\nabla T)_{\gamma,l,m}$ and $(\boldsymbol{v}\cdot\nabla\boldsymbol{v})_{\gamma,l,m}$ in the Boussinesq equations. Both of these nonlinear terms are a sum of many products of $T_{\gamma',l',m'}$, $\omega_{\gamma'',l'',m''}$, and $\psi_{\gamma''',l''',m'''}$. Since $T_{\gamma',l',m'}$, $\omega_{\gamma'',l'',m''}$, and $\psi_{\gamma''',l''',m'''}$ each peak at different radii, the advection terms and $T_{\gamma,l,m}$ can have small-scale radial structure.

g) Isotropy

Our measure of isotropy, $I(l, r)$, is plotted in Figures 14 and 15 for $l = 1$ and $l = 2$. Both curves have several grid points near $r = 0$; and as r goes to zero, $I(l, r)$ smoothly approaches 1 which shows the numerical code is accurate

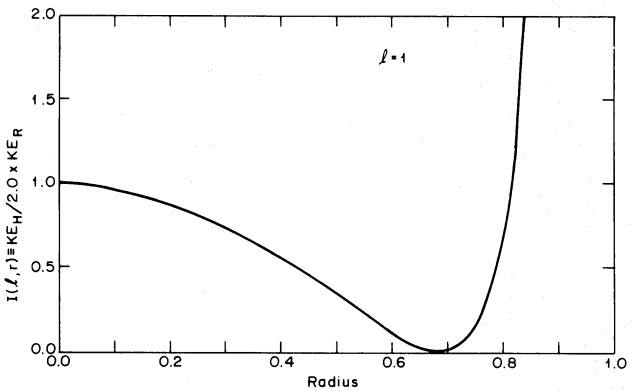

FIG. 14.—The ratio of the horizontal to the radial component of the kinetic energy for $l = 1$. The ratio is a measure of the large scale anisotropy of the flow.

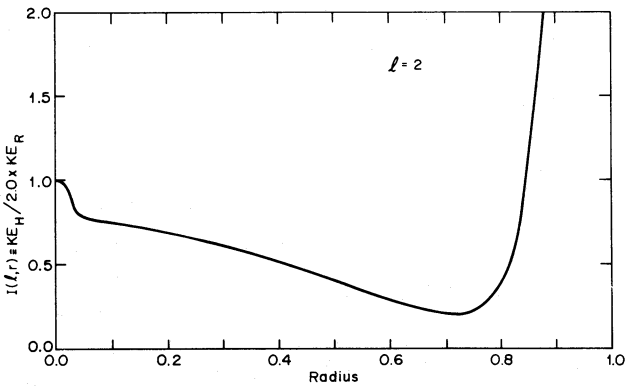

FIG. 15.—Same as Fig. 15 except that this figure is for the $l = 2$ component of the velocity. The anisotropy for $l = 2$ is qualitatively the same for $l > 2$, and there is no apparent isotropization of the velocity at small wavelengths.

near the origin (see § IV*f*). Figure 14 shows that the horizontal component of the $l = 1$ velocity goes to zero at $r = 0.67$ and then rapidly increases in the outer boundary layer. The obvious conclusion to be drawn from $I(l = 1, r)$ is that the large-scale structure of the convective velocity is markedly anisotropic.

We have illustrated $I(l = 2, r)$ because it is very similar to all of the $I(l, r)$ curves with $l > 1$. For $l > 1$, $I(l, r)$ diminishes with increasing radius (although it never goes to zero) and then increases in the boundary-layer. Because $I(l > 1, r)$ never goes to zero, we might argue that the velocity for modes with $l > 1$ is more isotropic than the velocity when $l = 1$. However, there is certainly no evidence for a "return to isotropy" in the small-scale modes. The lack of isotropy in the small scales is not surprising since there is not much of an energy cascade and the velocity (Reynolds number ~ 3) is far from being turbulent.

VI. DISCUSSION

We have computed the convective flow with a Prandtl number of 10 and with a Rayleigh number that is ~ 30 times the critical value. Despite a variety of initial three-dimensional configurations of the flow, the fluid always evolves to the same steady state with two orthogonal planes of reflection symmetry. This computation differs from previous studies of convection because the equations of motion have been used to determine the horizontal structure of the flow; an *a priori* horizontal structure was not imposed as a constraint to the equations of motion. We emphasize that an examination of only the large-scale modes is not adequate to determine the stability of a convective solution; it is necessary to include small-scale modes as well. One large-scale equilibrium solution may be unstable with respect to another large-scale equilibrium solution due to small wavelength perturbations. If the expansion of the equations of motion does not include these small modes, both equilibrium solutions will appear to be stable when in fact one is unstable. In our computations, we have included enough modes so that the largest of the perturbations has a viscous dissipation time scale that is $\sim 10^4$ times smaller than the dynamic time scale. It is therefore unlikely that the steady-state solution that we have computed is unstable with respect to any of the neglected small modes. The only other study of convection that has a spatial resolution equivalent to ours was done by Gilman (1978, and references cited therein). Unfortunately, it is impossible to make direct comparisons to Gilman's work because his calculation is for a rapidly rotating shell fluid in which the Coriolis force is roughly the same strength as the convective buoyancy.

Perhaps the most interesting result presented in this paper is that for the first time we have been able to calculate the kinetic and thermal energy spectra as functions of wavelength by solving the equations of motion alone. (For a somewhat similar derivation of a kinetic spectrum by use of an eddy viscosity, see Siggia and Patterson 1978.) We have seen that the kinetic energy is so quickly dissipated by viscosity that it does not have time to cascade from the large modes down to smaller modes. Since the thermal dissipation rate is slower than the viscous dissipation rate, it is reassuring that our calculations show that the thermal energy does have time to cascade down to smaller wavelength before it is dissipated.

I would like to thank Peter Gierasch for many useful suggestions that benefited this work. I also thank the National Center for Atmospheric Research (which is sponsored by the National Science Foundation) for use of the CRAY-1 computer.

APPENDIX

In this Appendix we show how to transform a temperature spectrum, $\mathrm{TE}(l, r)$, that is a function of the two-dimensional wavenumber and radius (cf. eq. [4.8]) to a spectrum that is a function of the three-dimensional

wavenumber, TE(k). The transform is not unique because the temperature is known only over a finite domain, and it is necessary to supplement the usual mathematical definition of the spectrum with an additional constraint on the correlation function.

The correlation of the temperature is defined:

$$C(\boldsymbol{r}) = \frac{1}{2}\int \tilde{T}(\boldsymbol{x})\tilde{T}(\boldsymbol{x}+\boldsymbol{r})dx^3 . \tag{A1}$$

The integral is over all space, but because $\tilde{T}(\boldsymbol{x})$ is defined only for $|x| \leq 1$, it is necessary to insert a window function, $W(\boldsymbol{x}, \boldsymbol{r})$, into the integral in equation (A2). The simplest choice for $W(\boldsymbol{x}, \boldsymbol{r})$ is

$$\begin{aligned} W(\boldsymbol{x}, r) &= 1 \quad \text{if } |x| \leq 1 \text{ and } |\boldsymbol{x}+\boldsymbol{r}| \leq 1 \\ &= 0 \quad \text{otherwise} . \end{aligned} \tag{A2}$$

There are several problems with this definition of the window function. If $\tilde{T}$ were independent of position, we would expect the correlation function to be independent of $\boldsymbol{r}$. Using equation (A3), we find that $C(\boldsymbol{r})$ decreases with increasing $|r|$. The decrease is due to the finite geometry and not due to an inherent property of $\tilde{T}$. The window function must be chosen to compensate for this effect. Another consideration in the choice of $W(\boldsymbol{x}, \boldsymbol{r})$ is that our integrations are numerical and T is represented on a radial grid with a truncated expansion in θ and ϕ. $W(\boldsymbol{x}, \boldsymbol{r})$ must be chosen so that $C(\boldsymbol{r})$ reflects the properties of $\tilde{T}$ and not the numerical representation of $\tilde{T}$.

It is convenient to have $W(\boldsymbol{x}, \boldsymbol{r} = 0) = 1$ so that

$$C(0) = 4\pi \int_0^1 \mathrm{TE}(r)r^2 dr . \tag{A4}$$

We define $\mathscr{C}(\boldsymbol{k})$ to be the Fourier transform of $C(\boldsymbol{r})$:

$$\mathscr{C}(\boldsymbol{k}) = (2\pi)^{-3}\int C(\boldsymbol{r}) \exp(-i\boldsymbol{k}\cdot\boldsymbol{r})dr^3 . \tag{A5}$$

Integrating $k^2\mathscr{C}(\boldsymbol{k})$ over all directions, we obtain the three-dimensional thermal energy spectrum that is a function of $k \equiv |\boldsymbol{k}|$:

$$\mathrm{TE}(k) = (2\pi)^{-2}\int d\Omega_r dr dx^3 \tilde{T}(\boldsymbol{x})\tilde{T}(\boldsymbol{x}+\boldsymbol{r}) \sin(kr) W(\boldsymbol{x}, \boldsymbol{r}) kr . \tag{A6}$$

By choosing $W(\boldsymbol{x}, \boldsymbol{r} = 0) = 1$ we find that the integral of TE(k) over all k is equal to the total fluctuating thermal energy:

$$\int_0^\infty \mathrm{TE}(k)dk = 4\pi \int_0^1 \mathrm{TE}(r)r^2 dr . \tag{A7}$$

If $W(\boldsymbol{x}, \boldsymbol{r}) \equiv 1$, then TE($k$) reduces to

$$\mathrm{TE}(k) = \tfrac{1}{2}(2\pi)^3 \int \tilde{T}_k \tilde{T}_{-k} k^2 d\Omega_k , \tag{A8}$$

where T_k is the Fourier transform of $\tilde{T}$. One final caution: since the spatial resolution is more limited in the horizontal than in the radial direction, and since the horizontal resolution is $\sim 2\pi[l_{\mathrm{cutoff}}(l_{\mathrm{cutoff}}+1)]^{-1/2}$, we should not expect TE(k) to be accurate for $k > [l_{\mathrm{cutoff}}(l_{\mathrm{cutoff}}+1)]^{1/2}$. Similarly TE($k$) will not be accurate for $k < 1$.

In terms of modes, equation (A6) becomes

$$\begin{aligned} \mathrm{TE}(k) = (2\pi)^{-1} &\int d\Omega_x d\Omega_r dr dx x^2 kr \sin(kr) W(\boldsymbol{x}, \boldsymbol{r}) \\ &\times \Bigg[\Bigg[\sum_l \Bigg\{\sum_{m\geq 1} [T_{R,l,m}(x) - iT_{I,l,m}(x)] Y^{l,m}(\theta_x, \phi_x) \\ &\quad + [T_{R,l,m}(x) + iT_{I,l,m}(x)](-1)^m Y^{l,-m}(\theta_x, \phi_x) + 2^{1/2} T_{R,l,0}(x) Y^{l,0}(\theta_x, \phi_x)\Bigg\} \\ &\times \sum_{l'} \Bigg\{\sum_{m'\geq 1} [T_{R,l',m'}(|\boldsymbol{x}+\boldsymbol{r}|) - iT_{I,l',m'}(|\boldsymbol{x}+\boldsymbol{r}|)] Y^{l',m'}(\theta_{x+r}, \phi_{x+r}) \\ &\quad + [T_{R,l',m'}(|\boldsymbol{x}+\boldsymbol{r}|) + iT_{I,l',m'}(|\boldsymbol{x}+\boldsymbol{r}|)](-1)^{m'} Y^{l',-m'}(\theta_{x+r}, \phi_{x+r})\Bigg\} \\ &+ 2^{1/2} T_{R,l',0}(|\boldsymbol{x}+\boldsymbol{r}|) Y^{l',0}(\theta_{x+r}, \phi_{x+r})\Bigg]\Bigg] . \end{aligned} \tag{A9}$$

The spherical coordinates of the vector $(\boldsymbol{x} + \boldsymbol{r})$ are θ_{x+r} and ϕ_{x+r}. We have chosen the north poles of the (θ_r, ϕ_r) and the $(\theta_{x+r}, \phi_{x+r})$ coordinate systems to lie along the $\boldsymbol{x}$ axis. Using the identity

$$\int Y^{l,m}(\theta_x, \phi_x) Y^{l',-m'}(\theta_{x+r}, \phi_{x+r}) d\Omega_x d\phi_r = 2\pi P_l[\cos(\theta_{x+r})]\delta_{ll'}\delta_{mm'} \tag{A10}$$

and assuming that W depends only on $|\boldsymbol{x}|$, $|\boldsymbol{r}|$, and the angle between $\boldsymbol{x}$ and $(\boldsymbol{x} + \boldsymbol{r})$, we find that the fluctuating thermal energy spectrum is

$$\mathrm{TE}(k) = 2\int d(\cos\theta_r) dr dx x^2 kr \sin(kr) W(x, r, \theta_{r+x}) \sum_{\gamma,l,m} [T_{\gamma,l,m}(x) T_{\gamma,l,m}(|\boldsymbol{x} + \boldsymbol{r}|) P_l(\cos\theta_{x+r}) . \tag{A11}$$

In equations (A10) and (A11) $P_l(\cos\theta_{x+r})$ is a Legendre polynomial, and

$$\cos(\theta_{x+r}) = (\boldsymbol{x}^2 + |\boldsymbol{x} + \boldsymbol{r}|^2 - \boldsymbol{r}^2)/(2x|\boldsymbol{r} + \boldsymbol{x}|) , \tag{A12}$$

$$|\boldsymbol{x} + \boldsymbol{r}| = (\boldsymbol{x}^2 + \boldsymbol{r}^2 + 2rx\cos\theta_r)^{1/2} . \tag{A13}$$

Not surprisingly, equation (A11) shows that TE(k) depends upon the product of $T_{\gamma,l,m}(|\boldsymbol{x}|)$ and $T_{\gamma,l,m}(|\boldsymbol{x} + \boldsymbol{r}|)$, but contains no cross terms between different modes.

When the flow is isotropic, the three-dimensional spectrum can be directly related to the two-dimensional spectrum. If, for example, we choose the window function such that $W = 1$ for $r \leq 2x$ and $W = 0$ otherwise, then equation (A11) reduces to

$$\mathrm{TE}(k) = 4\int dr dx x^2 kr \sin(kr) W(\boldsymbol{x}, \boldsymbol{r}) \sum_{\gamma,l,m} [T_{\gamma,l,m}(x)]^2 P_l(1 - \tfrac{1}{2}r^2/x^2) . \tag{A14}$$

Defining

$$d_l(kx) \equiv 8\int_0^{2xk} y \sin(y) P_l(1 - \tfrac{1}{2}y^2/k^2x^2) dy , \tag{A15}$$

we find that

$$\mathrm{TE}(k) = k^{-1}\int \sum_l r^2 \mathrm{TE}(l, r) d_l(kr) dr . \tag{A16}$$

REFERENCES

Busse, F. H. 1975, *J. Fluid Mech.*, **72**, 67.
Corrsin, S. 1964, *Phys. Fluids*, **7**, 1156.
Gilman, P. A. 1978, *Geophys. Ap. Fluid Dynamics*, **11**, 191.
Herring, J. R. 1963, *J. Atm. Sci.*, **20**, 325.
Lorenz, E. N. 1963, *J. Atm. Sci.*, **20**, 130.
Malkus, W. V. R., and Veronis, G. 1958, *J. Fluid Mech.*, **4**, 225.
Marcus, P. S. 1979, *Ap. J.*, **231**, 176 (Paper I).
———. 1980, *Ap. J.*, submitted.
Siggia, E. D., and Patterson, G. S. 1978, *J. Fluid Mech.*, **86**, 567.
Tennekes, H., and Lumley, J. L. 1972, *A First Course in Turbulence* (Cambridge, MA: MIT Press).
Toomre, J., Gough, D. O., and Spiegel, E. A. 1977, *J. Fluid Mech.*, **79**, 1.
Toomre, J., Zahn, J. P., Latour, J., and Spiegel, E. A. 1976, *Ap. J.*, **207**, 545.

PHILIP S. MARCUS: Center for Radiophysics and Space Research, Cornell University, Ithaca, NY 14853